

## On the origins of band topography, Europa

F. Nimmo,<sup>a,\*</sup> R.T. Pappalardo,<sup>b</sup> and B. Giese<sup>c</sup>

<sup>a</sup> Department of Earth Sciences, University College London, Gower St, London WC1E 6BT, UK

<sup>b</sup> Laboratory for Atmospheric and Space Physics, Campus Box 392, University of Colorado, Boulder, CO 80309, USA

<sup>c</sup> DLR, Rutherfordstrasse 2, 12489 Berlin, Germany

Received 14 May 2003; revised 17 July 2003

### Abstract

We use stereo-derived topography of extensional bands on Europa to show that these features can be elevated by 100–150 m with respect to the surroundings, and that the positive topography sometimes extends beyond the band margins. Lateral variations in shell thickness cannot maintain the observed topography for timescales greater than  $\sim 0.1$  Myr. Lateral density variations can maintain the observed topography indefinitely; mean density contrasts of 5 and 50 kg m<sup>-3</sup> are required for shell thicknesses of 20 and 2 km, respectively. Density variations caused by temperature contrasts require either present-day heating or that bands are young features ( $< 1$  Myr old). Stratigraphic analyses suggest that these mechanisms are unlikely. The observation that bands form from ridges may be explained by an episode of shear-heating on ridges weakening the ridge area, and leading to strain localization during extension. Fracture porosity is likely to persist over Myr timescales in the top one-third to one-quarter of the conductive part of the ice shell. Lateral variations in this porosity (of order 20%) are the most likely mechanism for producing band topography if the ice shell is thin ( $\approx 2$  km); porosity variations of 2% or less are required if the shell is thicker ( $\approx 20$  km). If the ice shell is thick, lateral variations in salt content are a more likely mechanism. Warm ice will tend to lose dense, low-melting temperature phases and be buoyant relative to colder, salt-rich ice. Thus, lateral density variations will arise naturally if bands have been the sites of either localized heating or upwelling of warm ice during extension.

© 2003 Elsevier Inc. All rights reserved.

*Keywords:* Satellites of Jupiter; Tectonics; Ices; Geological processes

### 1. Introduction

Jupiter's satellite Europa has been extensively deformed by tidal processes (e.g., Greenberg et al., 2002). Tidal heating (Ross and Schubert, 1987; Ojakangas and Stevenson, 1989) is probably also responsible for the presence of an ocean beneath Europa's solid ice shell (Kivelson et al., 2000). A particularly clear example of surface deformation is the class of features known as bands (Figs. 1, 2). Bands seen in Voyager images were described by Luchitta and Soderblom (1982) and Schenk and McKinnon (1989); the latter showed that pre-existing lineaments could be fit back together if the intervening dark bands were removed. More recent interpretation (Sullivan et al., 1998; Tufts et al., 2000; Prockter et al., 2002) of Galileo images

has confirmed that bands are typically regions separating relatively undeformed, previously adjacent areas. The bands are typically several up to 30 km wide and can be bounded by ridges. While the inferred motion across the bands is usually extensional, there is sometimes a component of lateral motion (Tufts et al., 2000) and possibly compression (Sarid et al., 2002; Schulson, 2002). The bands show internal structure, commonly possessing a medial valley, and sometimes showing symmetry about this valley reminiscent of sea-floor spreading on Earth (Sullivan et al., 1998; Prockter et al., 2002). The bands can be disrupted by chaos patches, and sometimes show V-shaped patterns of hummocks (Prockter et al., 2002). Bands are commonly cross-cut by later features, indicating that they vary in age. Younger bands tend to be darker and show surface contamination by a non-ice component (e.g., Geissler et al., 1998); older bands are brighter and look more similar to the background plains.

The mechanism by which bands formed is unclear. Extension is undoubtedly the dominant process, but the band material may originally have been water (Tufts et al., 2000)

\* Corresponding author. Current address: Department Earth and Space Sciences, UCLA, 595 Charles Young Drive E, Los Angeles, CA 90095-1567, USA.

E-mail address: [nimmo@ess.ucla.edu](mailto:nimmo@ess.ucla.edu) (F. Nimmo).

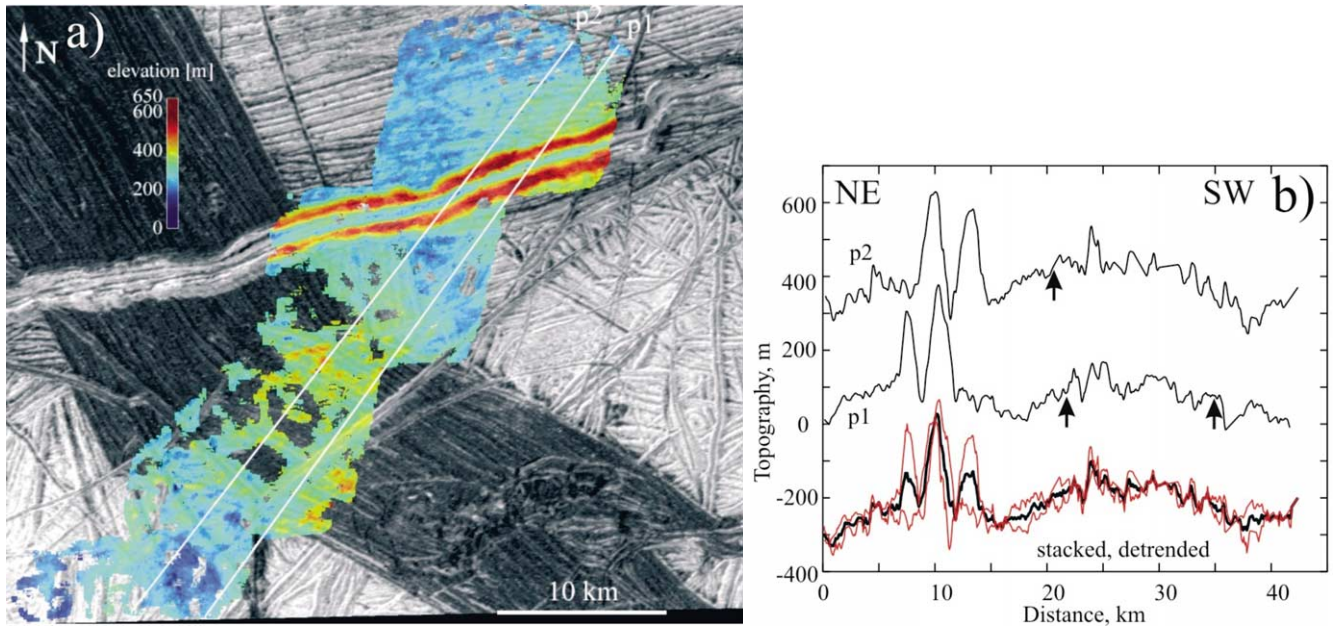


Fig. 1. (a) Background image is of “Wedges” terrain, from Galileo’s 12th orbit, resolution  $70 \text{ m pixel}^{-1}$ , centred at  $16^\circ \text{ S}$ ,  $164^\circ \text{ E}$ . Coloured data is stereo-derived topography obtained from the background image and four  $32 \text{ m pixel}^{-1}$  Galileo images from the same orbit (see Prockter et al., 2002). Vertical uncertainty is 20 m and horizontal resolution is 400–800 m. Note that dark band appears to have positive topography with respect to the surroundings. (b) Plot of topography as a function of distance. Thin dark lines are topographic profiles p1, p2 (for location see (a)), interpolated to 70 m, smoothed using a moving 3-point average and offset for clarity. Bold dark line is stacked profile, thin red lines are  $\pm$  one standard deviation  $\sigma$ . Stacked profile was detrended using least-squares regression prior to plotting. Position of zero elevation is arbitrary. Arrows denote approximate edge of the dark band (profile p2 lacks one arrow because the edge of the band is uncertain). Vertical exaggeration is 33 : 1.

or upwelling warm ice (Sullivan et al., 1998; Prockter et al., 2002). An important observation is that bands commonly stand high relative to their surroundings (Tufts et al., 2000; Prockter et al., 2002). In this paper we first characterize band topography based on the limited stereo observations available. We then examine possible mechanisms responsible for this topography and the light these mechanisms may throw on band formation. Mathematical derivations are given in Appendices A and B.

## 2. Observations

Figures 1 and 2 show images of the three bands we study, and the associated stereo-derived topography. More details on the stereo technique may be obtained from Giese et al. (1998) and the figure captions. The structure and inferred history of these three bands have been described in detail by Tufts et al. (2000) and Prockter et al. (2002). Here we briefly describe the relevant details.

Figure 1a shows a portion of a prominent dark band that has been examined and described by several researchers (Schenk and McKinnon, 1989; Sullivan et al., 1998; Tufts et al., 2000; Prockter et al., 2002; Schulson, 2002). The band is wedge-shaped overall, tapering toward its southeastern end. Pre-existing features can be reconstructed by removing the band, demonstrating an (at least locally) extensional nature (Sullivan et al., 1998; Tufts et al., 2000;

Prockter et al., 2002). A central trough, rough bilateral symmetry, and apparent spreading apart of superimposed structures argues for a mid-ocean ridge analogue process in forming the band (Sullivan et al., 1998; Prockter et al., 2002). Schulson (2002) argues that this feature is analogous to a “wing-crack” formed in response to regional compressive stresses; nonetheless, local extension would be responsible for opening the band even in such a model. The band is stratigraphically recent relative to others in the region, but it is crossed by several younger ridges (Prockter et al., 1999, 2002).

Stereo imaging occurs at the band’s dog-leg bend, where the feature is 18 km in width. Previous work has noted that this band stands high relative to its surroundings (Tufts et al., 2000; Prockter et al., 2002). Our topographic profiles indicate that the band has topographic relief of  $\approx 100 \text{ m}$ , and that the convex topographic swell associated with the band appears to extend beyond the band’s lateral boundaries into the surrounding ridged plains (Fig. 1b). Despite gaps in the topographic data, it is also apparent that there are variations in band topography along-strike, with the band elevation less pronounced towards the NW.

The dark band of Fig. 2a (Lineament E of Tufts et al. (2000)) is  $\approx 3 \text{ km}$  wide. It displays finely spaced lineaments and no central trough or obvious bilateral symmetry. Its low albedo and cross-cutting relationships suggest that this band is relatively young. Within the area of stereo coverage, this dark band is intersected by a very narrow ( $\approx 1 \text{ km}$ ) dark

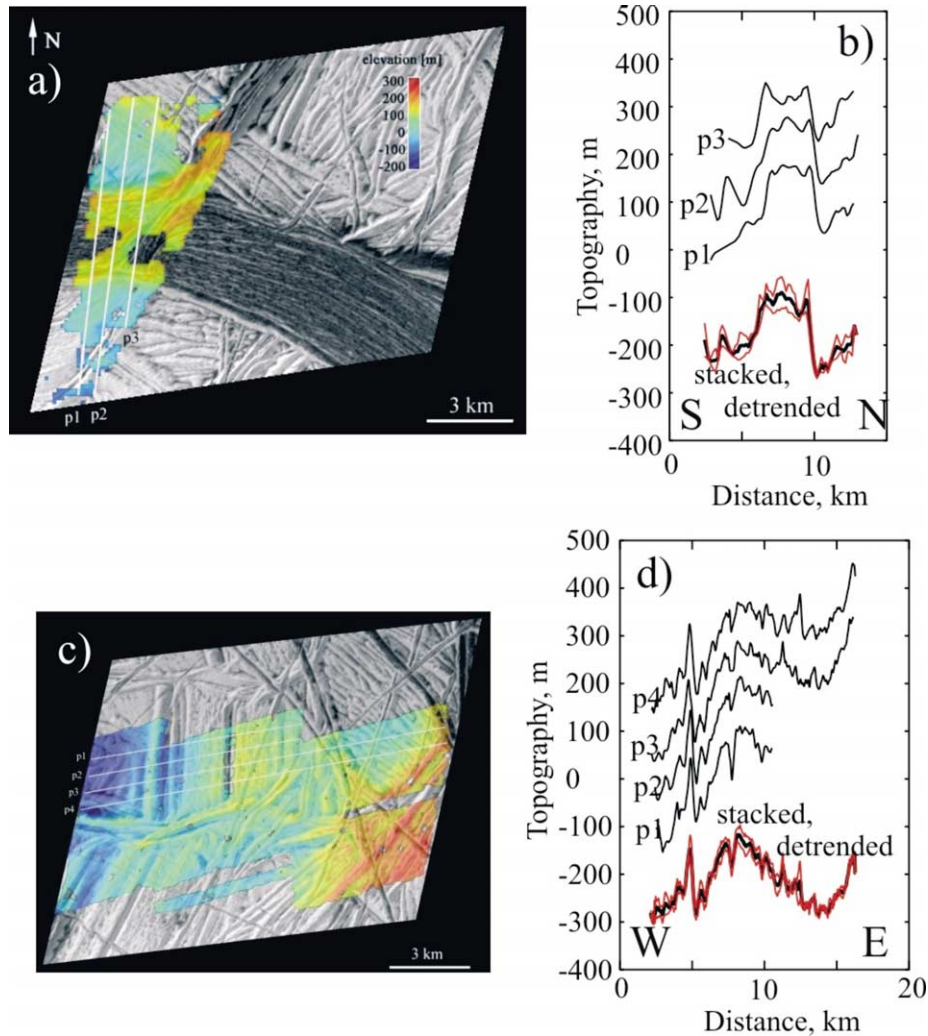


Fig. 2. (a) Background image is from Galileo’s 12th orbit, resolution  $32 \text{ m pixel}^{-1}$ , centred at  $18^\circ \text{ S}$ ,  $163^\circ \text{ E}$ . Coloured data is stereo derived topography obtained from the background image and an  $80 \text{ m pixel}^{-1}$  Galileo image from the same orbit. Vertical uncertainty is 20 m, horizontal resolution 400–800 m. (b) Plot of topography as a function of distance. Thin dark lines are topographic profiles p1–p3 (for location see (a)), interpolated to 150 m, smoothed using a moving 3-point average and offset for clarity. Profiles are aligned on steep N scarp. Bold dark line is stacked profile, thin red lines are  $\pm$  one standard deviation  $\sigma$ . Stacked profile was detrended using least-squares regression prior to plotting. Position of zero elevation is arbitrary, vertical exaggeration as for Fig. 1b. (c) Background image is from Galileo’s 12th orbit, resolution  $32 \text{ m pixel}^{-1}$ , centred at  $17^\circ \text{ S}$ ,  $164^\circ \text{ E}$ . Coloured data is stereo-derived topography obtained from the background image and three  $16 \text{ m pixel}^{-1}$  images (see Prockter et al., 2002). Vertical uncertainty is 10 m, horizontal resolution 150–300 m. (d) Same as for (b), except that interpolation distance is 30 m and profiles are aligned on prominent ridge at East end of profiles.

band, which may have been active near-simultaneously (Patterson and Head, 2003). The topography of Fig. 2b shows that the band has steep boundaries, a plateau-like profile, and stands  $\approx 100\text{--}150$  m above the surrounding terrain. The band of Fig. 2c (Ridge C2 of Tufts et al. (2000), and Band B of Prockter et al. (2002)) display a prominent medial trough and hummocky, weakly lineated texture. The  $\approx 8$  km wide band is bright and is segmented along its length by other more recent structures, both implying that it is a relatively old feature (Prockter et al., 2002). Topographic profiles (Fig. 2d) show that the band is convex with  $\approx 150$  m of topography. The associated topographic swell appears to extend beyond the band’s western boundary as marked by a well-defined ridge, and into the surrounding ridged plains.

The characteristics of the three bands studied here may be summarized as follows:

- (1) All three bands show positive topography in the range 100–150 m relative to the surroundings.
- (2) The positive topography appears to extend beyond the edge of the band in at least some cases.
- (3) The positive topography is associated with both stratigraphically young and older bands.
- (4) All bands contain sub-parallel ridges 50–100 m wide and aligned with the margins.

In the next section, we will consider possible mechanisms for creating the positive topography associated with bands. We will concentrate on the mean positive topography, rather

than its variation along strike, as it is the former observation that is likely to provide more insight into processes within Europa's ice shell.

### 3. Models for topographic support

Topography on Earth is generally supported by a combination of rigidity (flexure) and lateral contrasts in crustal thickness or density (isostasy). The latter may be due to thermal or compositional processes, and may be either static (e.g., continental shields) or dynamic (e.g., the Hawaiian swell). Similar processes may be operating on Europa (Schenk and McKinnon, 2001).

For situations in which the lithosphere has no rigidity, the topography  $h$  relative to a zero-elevation reference state is given by (e.g., Turcotte and Schubert, 1982)

$$h = t_c \left( \frac{\Delta\rho}{\rho'} \right) + w \left( \frac{\rho_w - \rho'}{\rho'} \right), \quad (1)$$

where  $t_c$  is the reference crustal thickness,  $\Delta\rho = \rho - \rho'$ ,  $\rho$  is the (vertically averaged) reference shell density,  $\rho'$  is the vertically averaged shell density of interest,  $\rho_w$  is the density of the sub-shell material and  $w$  is the thickness of the crustal root.

Previous work (Tufts et al., 1997; Williams and Greeley, 1998; Billings and Kattenhorn, 2002; Figueredo et al., 2002; Nimmo et al., 2003) suggests that the near-surface ice may have an appreciable rigidity  $D$ . This rigidity reduces the amplitude of the isostatic shell deflection. The deflection  $s$  of an elastic plate under a periodic load resulting in topography  $h$  is given by (Turcotte and Schubert, 1982)

$$s = \frac{h\rho}{(Dk^4/g) + \rho_w - \rho}, \quad (2)$$

where  $g$  is the acceleration due to gravity and  $k$  is the load wavenumber. For  $D = 0$ , this equation reduces to that given by Eq. (1) when  $\Delta\rho = 0$ . Similar equations can be derived for the case when the load applied has a different density to the shell material. The rigidity  $D$  is given by

$$D = \frac{ET_e^3}{12(1-\nu^2)}, \quad (3)$$

where  $E$  is the Young's modulus,  $\nu$  is the Poisson's ratio and  $T_e$  is the effective elastic thickness.

Below we consider various possibilities for topographic support in more detail. We will assume that  $\rho = 900 \text{ kg m}^{-3}$  and  $\rho_w = 1000 \text{ kg m}^{-3}$ . While both these values are uncertain due to the possible presence of contaminants (e.g., Kargel et al., 2000) and/or porosity, it is the density contrast between solid and liquid that is most important. The density contrast is unlikely to exceed  $100 \text{ kg m}^{-3}$ , since pure water ice has a density at 260 K of  $917 \text{ kg m}^{-3}$  (Kirk and Stevenson, 1987). Thus using  $\rho = 900 \text{ kg m}^{-3}$  results in lower bounds on quantities such as the porosity or shell thickness variation required to produce the observed topography. In some situations, we have to assume a shell thick-

ness, the value of which is uncertain. There are several lines of evidence suggesting that  $t_c \approx 20 \text{ km}$  (McKinnon, 1999; Schenk, 2002; Turtle and Ivanov, 2002; Nimmo et al., 2003), but alternative, thinner shell ( $t_c \approx 2\text{--}6 \text{ km}$ ) scenarios also exist (Hoppa et al., 1999; Greenberg et al., 2000; O'Brien et al., 2002). We explore both sets of values where appropriate.

#### 3.1. Shell thickness variations

When  $\Delta\rho = 0$  in Eq. (1), all topographic variations are supported by lateral shell thickness changes (Airy isostasy). For ice, the amplitude of the root  $w$  is  $\rho/(\rho_w - \rho) \approx 10$  times the topography  $h$ . Thus, 100–150 m topography requires a root of 1–1.5 km thickness to support it, irrespective of the mean shell thickness.

The presence of lateral thickness variations produces pressure gradients which can cause the ductile ice near the base of the shell to flow. Stevenson (2000) has argued that this flow is rapid enough that lateral shell thickness variations are unlikely to persist on Europa for more than  $10^2\text{--}10^5$  years, depending on shell thickness. Conversely, O'Brien et al. (2002) argue that the shell thickness changes at rates of  $0.1\text{--}10 \text{ km Myr}^{-1}$  for  $t_c = 6 \text{ km}$ , implying that lateral thickness contrasts may persist for  $10^5\text{--}10^7$  years. Buck et al. (2002) reached similar conclusions.

The above papers assume a Newtonian viscosity, while that of ice is likely to be non-Newtonian (Goldsby and Kohlstedt, 2001). Appendix A takes a similar approach to that of Bird (1991) and derives an approximate timescale for non-Newtonian flow to remove shell thickness variations. Figure 3 plots this relaxation timescale as a function of ice shell thickness and the wavelength of the thickness variation.

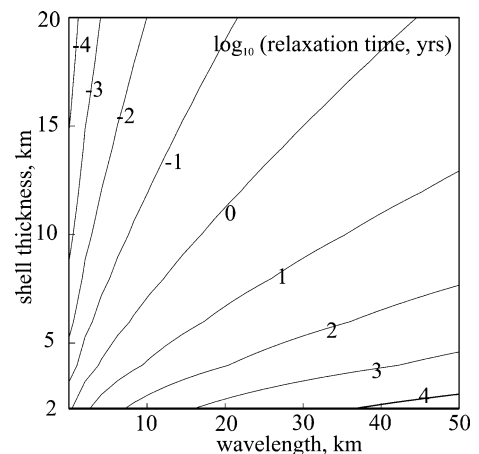


Fig. 3. Contour of timescale for lower crustal flow as a function of ice shell thickness and topographic wavelength. The method and variables are defined in Appendix A. Surface and base temperatures were 100 and 260 K, respectively; rheological parameters are for grain-boundary sliding (Goldsby and Kohlstedt, 2001):  $Q = 60 \text{ kJ mol}^{-1}$ ,  $n = 2.4$ , and  $A = 6 \times 10^{-7} \text{ Pa}^{-n} \text{ s}^{-1}$ . The initial amplitude of the shell thickness variation was 1 km, ice thermal conductivity varies as  $567/T$  (Klinger, 1980),  $g = 1.3 \text{ m s}^{-2}$ . The minimum shell thickness examined was 2 km.

It shows that even at the lowest shell thicknesses (2 km) and longest wavelengths (50 km) considered, lateral shell thickness contrasts cannot survive more than 0.1 Myr. Nimmo (2003) carried out a numerical study of the same problem and reached the same conclusion. Since the mean surface age of Europa is  $\approx 30\text{--}80$  Myr (Zahnle et al., 2003), we conclude that shell thickness variations are unlikely to be responsible for the observed band topography.

The results are similar to those of Stevenson (2000) but produce shorter flow timescales than O'Brien et al. (2002). We note that planetary scale lateral thickness variations due to spatial variations in tidal heating (Ojakangas and Stevenson, 1989) may persist owing to the large flow timescale for long wavelengths.

### 3.2. Density variations

If the shell thickness is constant, as argued above, then topography may instead be supported by lateral density variations (Pratt isostasy). Setting  $w = 0$  in Eq. (1), topography of 100 m requires  $\Delta\rho = 5 \text{ kg m}^{-3}$  for  $t_c = 20$  km, and  $\Delta\rho = 50 \text{ kg m}^{-3}$  for  $t_c = 2$  km. There are at least three possible causes of such a density contrast, which we will term active thermal, passive thermal, and compositional.

#### 3.2.1. Active thermal support

Active thermal density differences occur when there is a heat source located within the shell which can maintain the temperature structure. One such mechanism is linear diapirism (Head et al., 1999), which may be driven by localized tidal heating. As we discuss below, we think a likely

mechanism is shear heating, which was discussed in detail by Nimmo and Gaidos (2002). Figure 4a plots the steady-state temperature in excess of the background conductive heat profile obtained using the method of these authors. Heating occurs by brittle deformation in the top 2 km and by viscous dissipation beneath. The model includes a reduction in viscosity as the melting temperature is approached, which tends to buffer the temperature excess to  $< 100$  K. The density contrast at any point is given by

$$\Delta\rho = \rho\alpha\Delta T, \quad (4)$$

where  $\alpha$  is the thermal expansivity (here assumed to be  $1.4 \times 10^{-4} \text{ K}^{-1}$  (Kirk and Stevenson, 1987)) and  $\Delta T$  is the temperature excess. Vertical integration and use of Eq. (1) allows the isostatic topography to be calculated, which is shown in Fig. 4b. The theoretical profile has a similar shape to the observed profiles, and produces topography of 90 m amplitude, similar or slightly smaller to that observed. Increasing the depth of the brittle zone might increase the topographic amplitude slightly, but the buffering by melting will limit the increase. Furthermore, a deeper brittle zone would increase the lateral extent of positive topography and make the narrower bands (Figs. 2b, 2d) harder to fit. Thus, this mechanism alone is marginally acceptable for an ice shell thickness of 20 km (but see below). For thinner ice shells, the vertically integrated density contrast will be reduced, and the topography correspondingly smaller.

Conventional diapirism has a similar problem in producing the observed topography, because in strongly temperature-dependent convection  $\Delta T$  is controlled by the rheological properties of ice and is typically  $\approx 10$  K (McKinnon,

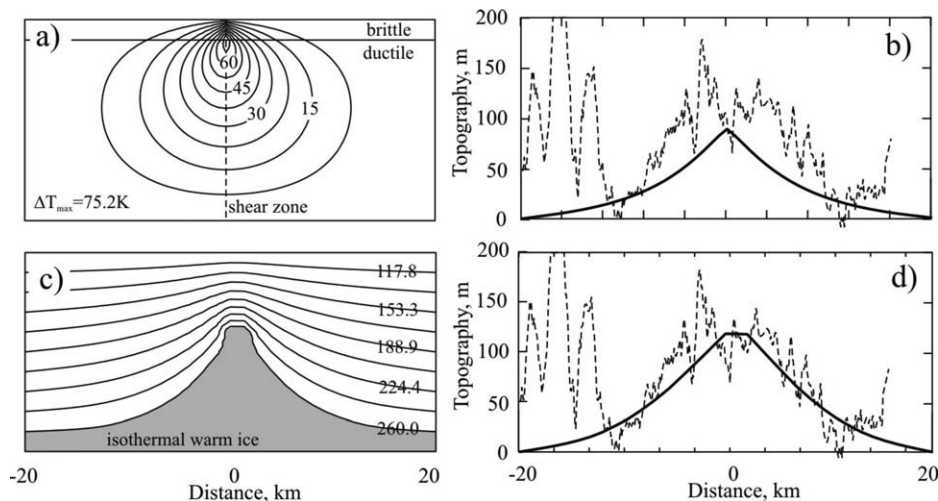


Fig. 4. Comparison of observed topography with models. (a) Contours of temperature in excess of background conductive gradient due to shear heating (see text). Domain is 40 km horizontally and 20 km vertically. Brittle layer thickness is 2 km, velocity contrast across shear zone  $8 \times 10^{-7} \text{ m s}^{-1}$ , other parameters from Nimmo and Gaidos (2002), Fig. 2. Contour interval 7.5 K. (b) Bold line is topography resulting from temperature distribution from (a), assuming isostatic compensation and a thermal expansivity of  $1.4 \times 10^{-4} \text{ K}^{-1}$ . Dashed line here and in (d) is topography from Fig. 1b for comparison. (c) Contours of temperature after 7.62 Ma of extension (see text) using the method of White and Bellingham (2002), size of domain as for (a). Initial temperature profile was conductive, with top and bottom at 100 K and 260 K, respectively. Peak (constant) strain rate is  $3 \times 10^{-15} \text{ s}^{-1}$  with Gaussian half-width 5 km. The maximum stretching factor is 1.86. Shaded region is assumed to be isothermal warm ice which has flowed to keep the base of the shell flat. (d) Bold line is topography resulting from temperature distribution from (c), assuming isostatic compensation. Note that if shaded region in (c) were water rather than isothermal ice, the topography would be negative owing to the higher density of water relative to ice.

1999; Nimmo and Manga, 2002). It is possible that  $\Delta T$  could be increased by tidal heating (Sotin et al., 2002), but it is not clear that the long-wavelength tidal deformation will couple efficiently with short-wavelength convective features (Moore, 2001).

### 3.2.2. Passive thermal support

Passive thermal density differences may arise when warm material is advected towards the surface during a rifting event. Figure 4c depicts a kinematic model of such a rifting event, using the forward model of White and Bellingham (2002). In this model the lateral strain rate variation is specified *a priori* and the resulting advection and diffusion of heat is solved using a finite-difference approach with variable grid spacing in the  $x$ -direction. The base of the advected material is set at 260 K and we assume zero rigidity, in agreement with terrestrial observations (e.g., Wood and Barton, 1983). It is assumed that lower shell flow is sufficiently rapid that the base of the shell remains at a constant depth (Appendix A); the upwardly advected material is replaced by warm, isothermal ice. If this lower shell flow does not occur and the upwardly advected material is replaced by water, the effect will be to generate negative surface topography, since water is considerably denser than ice. Figure 4d shows the topography resulting from this model, calculated as for Fig. 4b by taking the vertically integrated temperature contrast. The amplitude of the topography roughly matches the elevation of the observed bands, and will increase as the extension increases. Non-zero rigidity would reduce the topography, by  $\approx 50\%$  for an elastic thickness of 1 km. We further discuss the effect of rigidity on a simplified geometry below. The width of the anomaly is a free parameter and can be adjusted as needed to fit the observations.

Although we have only investigated one specific mechanism of passive thermal support, all such mechanisms suffer from the same problem: passive thermal density differences will only persist for a timescale  $\tau$  given by (see, e.g., Turcotte and Schubert, 1982)

$$\tau \sim d^2/\kappa, \quad (5)$$

where  $\kappa$  is thermal diffusivity and  $d$  is a characteristic length scale. For high degrees of extension, as is thought to occur for bands, warm isotherms may reach within a few km of the surface (see Fig. 4c). Taking  $\kappa = 10^{-6} \text{ m}^2 \text{ s}^{-1}$  for ice (Klinger, 1980), a typical timescale is thus  $\sim 1$  Myr, which is much shorter than the mean surface age of Europa of about 60 Myr (Zahnle et al., 2003). Thus, only if high-standing bands are very recent features is passive thermal support a viable option.

### 3.2.3. Compositional support

Compositional density differences occur if there are pores that are empty or filled with a denser contaminant such as salts (e.g., Kargel et al., 2000) or non-ice impact debris (e.g., Pierazzo and Chyba, 2002). If the mean non-ice volume frac-

tion is  $\phi$ , then we may write

$$\Delta\rho = \phi(\rho - \rho_s), \quad (6)$$

where  $\rho_s$  is the density of the non-ice material (zero if the pores are empty). Because the bands are high, they must either contain less non-ice material or more voids than the surrounding material. As argued above, the observed topography requires that  $\Delta\rho = 5$  to  $50 \text{ kg m}^{-3}$  for ice shell thicknesses of 20 to 2 km, respectively.

An attractive aspect of the compositional buoyancy argument is that it does not suffer from the lateral flow problem that bedevils Airy isostasy (see Section 3.1 above). Unlike Airy isostasy, there is no requirement for lateral pressure (density) contrasts to extend all the way to the base of the shell. These pressure gradients will still exist, but at shallow levels the ice is too cold for flow to be significant. Thus, shallow lateral density contrasts can create topography which will survive for geological timescales, unlike shell thickness contrasts.

Figure 5a shows a simplified density structure, consisting of a block of low density material surrounded by higher density material, which could create the observed topography. Figures 5b–5d show the resulting topography, modified by a near-surface layer of varying elastic thickness  $T_e$  (Eqs. (2) and (3)), for different block widths. As  $T_e$  increases, the width of the uplifted zone increases, but the amplitude of the topography decreases. The data from Fig. 1b is reasonably well fit by a block of 10 km width and  $T_e = 1$  km (Fig. 5b). The topographic uplift extends beyond the width of the low-density band, in agreement with surface observations. The narrower bands of Figs. 2b and 2d are better fit by a  $T_e$  of 0.1–0.3 km (Figs. 5c, 5d).

Thus, while it is clear that lateral density variations can cause the observed topography, the cause of these variations is less clear. Below we discuss the role of contaminants and fracture porosity on the possible ice density structure. We also discuss a plausible hybrid mechanism which could cause permanent compositional buoyancy by transient heating.

*Contaminants.* Pierazzo and Chyba (2002) estimate that  $5.5 \times 10^4 \text{ kg yr}^{-1}$  of cometary material is delivered to Europa. Although there may be a factor of 5 uncertainty in this estimate, such a rate of delivery is many orders of magnitude too small to affect Europa's ice shell density structure over 50 Myr. Conversely, variations in shell density due to the presence or absence of salts is likely to be important. Hydrated sulfates are inferred from near-infrared observations of the surface of Europa (McCord et al., 1999; Carlson et al., 1999), and salts are likely to be present in its ocean and ice shell (Kargel et al., 2000; Zolotov and Shock, 2001; Fanale et al., 2001). Hydrated sulfates have higher densities than water ice. For example, natron ( $\text{Na}_2\text{CO}_3 \cdot 10\text{H}_2\text{O}$ ), suggested on the basis of spectrometer measurements (McCord et al., 1999) has a density of  $1440 \text{ kg m}^{-3}$ . Thus, band

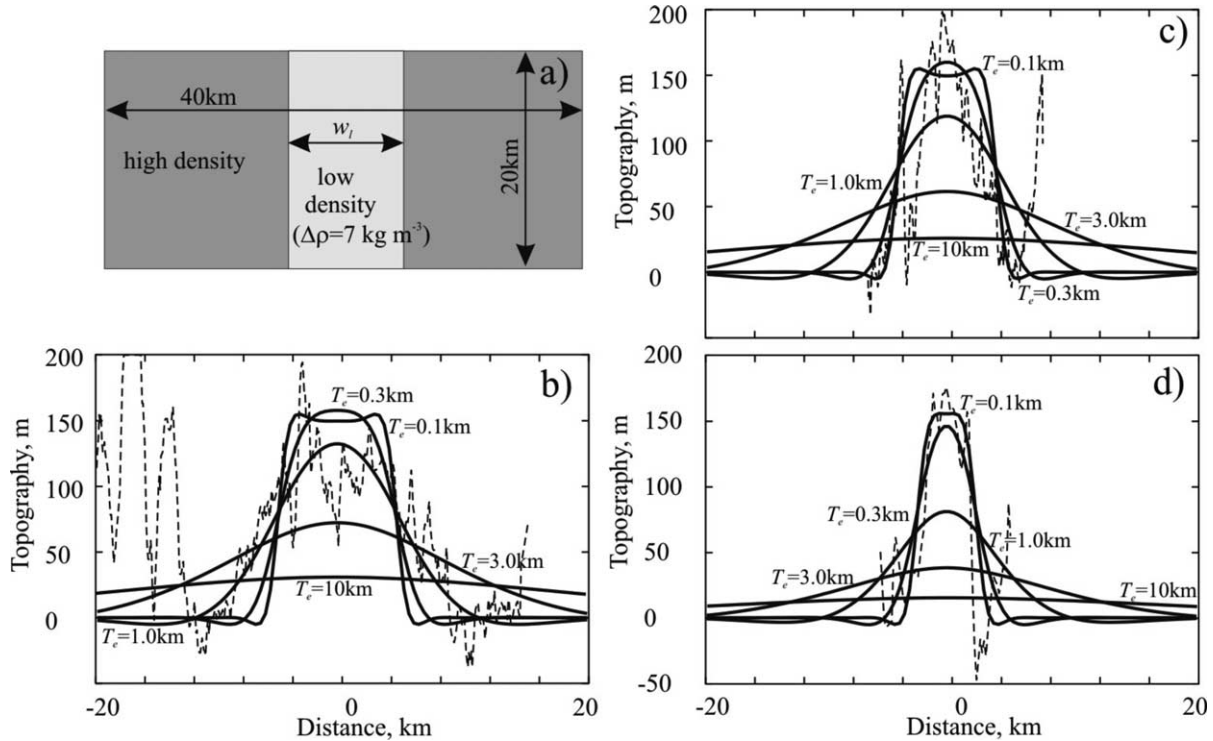


Fig. 5. (a) Sketch of geometry for topography caused by lateral density contrast (see text). (b) Solid lines are topography resulting from situation in (a) with  $w_l = 10$  km for different values of elastic thickness  $T_e$ , calculated using method based on Eqs. (2) and (3). Young's modulus 1 GPa, Poisson's ratio 0.25; computational domain extended from  $-60$  km to  $+60$  km. Dashed lines are data from Fig. 1b. (c) As for (b) but  $w_l = 8$  km and data from Fig. 2d. (d) As for (b) but  $w_l = 5$  km and data from Fig. 2b.

topography could be a result of bands containing lower salt concentrations than their surroundings.

Tufts et al. (2000) suggest that bands may form by freezing water, which might cause a decrease in density relative to the surroundings by excluding salts from the ice. However, Fanale et al. (2001) showed experimentally that rapid freezing of a putative European ocean does not create appreciable fractionation of cations or anions between solid and liquid. Furthermore, multispectral images of the surface (Geissler et al., 1998) suggest that the band surfaces are *more* contaminated than the surroundings. Unfortunately, the nature, density and depth extent of this contaminant are unknown, so it is not clear whether this observation contradicts the hypothesis that bands are elevated due to exclusion of salts during freezing. As we will argue below, another possibility is that local, thermally-driven removal of subsurface salts may be responsible for band topography.

**Fracture porosity.** Bands show lineated ridges and troughs (Figs. 1a, 2a) that suggest deformation and fracturing (Prockter et al., 2002), so fracture porosity is likely. Furthermore, if the bands are composed of crushed ice, as suggested by Tufts et al. (2000), it is very likely that the band ice will be more porous and thus less dense than the surrounding material. We may calculate the porosity required to account for the observed band topography as follows.

Near-surface ice will be cold and brittle, while deeper ice will flow in a viscous fashion to remove porosity. We

will therefore assume a near-surface layer of thickness  $z_\phi$  in which a constant excess porosity (relative to the surroundings) of  $\phi$  exists, with zero excess porosity below this level. Although more complex porosity models exist (e.g., Kosacki and Leliwa-Kopystynski, 1993; Eluszkiewicz, submitted), existing uncertainties are such that these models are unlikely to provide further insight. Compared with a neighbouring area of uniformly zero excess porosity, the elevation of a porous area (from Eqs. (1) and (6)) is simply

$$h = \phi z_\phi. \quad (7)$$

The rate of pore closure depends on the (Newtonian) ice viscosity and overburden pressure (Fowler, 1985). Using the equations outlined in Appendix B, we can obtain a porosity profile (relative to the initial porosity) at any subsequent time. Figure 6 shows the porosity profiles at 10 Myr for a variety of likely ice rheologies (Goldsby and Kohlstedt, 2001). Here we have assumed a conductive shell thickness of 6 km, appropriate to the thick-shell case when convection is occurring (e.g., McKinnon, 1999). We have adopted a timescale of 10 Myr since some bands are relatively recent features. The viscosity of ice near its melting point is  $10^{13} - 10^{15}$  Pa s (Pappalardo et al., 1998) and the activation energy is  $50 - 60$  kJ mol $^{-1}$  (Goldsby and Kohlstedt, 2001).

Figure 6 shows that  $z_\phi$  extends one-quarter to one-third of the conductive shell thickness, and is relatively insensitive to likely variations in activation energy or viscosity. Increasing  $\tau$  to 50 Myr causes a 20% reduction in  $z_\phi$ . The porosity

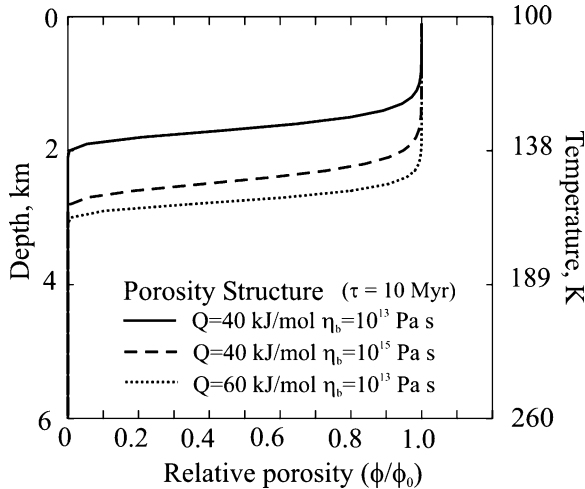


Fig. 6. Porosity profile (relative to initial porosity  $\phi_0$ ) after 10 Myr, calculated using the method of Appendix B. Surface and base temperatures and thermal conductivity same as for Fig. 3; conductive shell thickness 6 km.  $Q$  is activation energy and  $\eta_b$  is the viscosity at the base of the conductive shell.

depth is nearly proportional to the conductive shell thickness, because viscosity varies with depth much more rapidly than does pressure (see Appendix B, Eq. (B.3)). In general, brittle failure can occur at depths greater than  $z_\phi$ , but the results shown here suggest that fractures thus created will tend to close rapidly unless they are close to the surface.

Taking a value for  $z_\phi$  of 2 km, appropriate to the convecting thick shell case, Eq. (7) shows that the mean excess porosity required to produce the observed topography is 5%. For a 20 km thick shell which is conductive throughout,  $z_\phi$  would be 5–7 km and the excess porosity required 1.5–2%. For an ice shell thickness of 2 km,  $z_\phi$  will be 500–670 m, requiring a mean excess porosity of 15–20%. Hence, thin ice shells require large near-surface excess porosities to produce the observed topography; unfortunately, it is not yet clear whether near-surface porosity variations of order 20% are possible in icy satellites (Kossacki and Leliwa-Kopystynski, 1993).

**Thermally driven salt loss.** While thermal support is a potential mechanism for causing band topography, either the bands must be very recent (Section 3.2.2) or there must be a permanent heat source (Section 3.2.1). Here we consider one consequence of temporarily elevated temperatures which may contribute towards band topography: thermally driven variations in salt content.

Although hydrated sulfates have been inferred to exist at the surface of Europa (McCord et al., 1999; Carlson et al., 1999), their abundance in the bulk ice shell is unknown. Kargel et al. (2000) calculated equilibrium densities and mineralogies for various freezing products of a model European ocean. A eutectic liquid with melting point 268 K and density  $1200 \text{ kg m}^{-3}$  is the first to be produced when most of these compositions melt. Being denser than any likely solid phase, this liquid will drain downwards, leaving behind a

relatively buoyant residue. The draining timescale will be geologically rapid ( $\sim 10^3$  yrs for melt fractions of order 1% (Gaidos and Nimmo, 2000)). Since the draining of salts only occurs in relatively warm ice, this model does not contradict the observation that band surfaces appear to be more contaminated than the surroundings (Geissler et al., 1998). We also note that while the example liquid quoted here has a melting temperature only 5 K lower than that of pure water ice, other plausible compositions can have melting temperatures as low as 211 K (Kargel et al., 2000). There is thus a general tendency for ices which are near the melting point of pure ice to lose any dense salt contaminants, and thus become compositionally buoyant.

For an initial ice shell density of  $1000 \text{ kg m}^{-3}$  and thickness 20 km, removing 2.5% by volume of the example eutectic liquid would be sufficient to create the observed band topography. However, for a 2 km thick shell, the amount required is 25%, an implausibly high figure. Thus, this mechanism is only likely to work for relatively thick ice shells. As noted above, topography supported by compositional density differences is stable over Gyr timescales, unlike that supported by crustal roots or passive thermal processes.

Compositional buoyancy caused by salt loss is a likely outcome of the processes depicted in Figs. 4a and 4c. In Fig. 4a, brines will drain out of the heated area, resulting in a local increase in buoyancy and contributing to the positive topography. In Fig. 4c, the upwardly advected warm ice is likely to be relatively salt-poor, simply because it is close to the melting temperature, and also probably formed more slowly than near-surface ice. Thus, the upwelling ice will initially be both compositionally and thermally buoyant; the thermal component of topography will decay with time, but the compositional component will be long-lived. The scenario of Fig. 4c is also attractive because such upward advection of warm ice is a natural consequence of extension, and most bands appear to be primarily extensional. Finally, since the magnitude of the effect depends on the initial salt content of the ice shell, which may well be heterogeneous, it would not be surprising if the resulting topography varies spatially.

## 4. Discussion

### 4.1. Implications for shell thickness and activity

If the ice shell is thin ( $\approx 2$  km), the most viable mechanism for producing band topography appears to be  $\approx 20\%$  fracture porosity. Lateral shell thickness contrasts are not geologically sustainable, and neither salt-related nor thermal buoyancy are likely to be able to match the observed topography. The cyclic compression model of Tufts et al. (2000) is likely to result in bands with high porosity and is a viable explanation for band topography.

If the ice shell is thicker, smaller lateral density variations are required to produce the same topography. Thus, active

thermal support is an additional plausible mechanism, assuming that heating continues today. Passive thermal support only works if the bands are recent (Section 3.2.2). Because bands have a wide range of stratigraphic ages (Prockter et al., 1999; Figueredo and Greeley, 2003), passive thermal support is unlikely and active support only possible if present-day heating does not involve significant resurfacing. Either active or passive thermal mechanisms could result in lateral variations in density due to loss of salt-rich, low-melting temperature components. This compositional density contrast can sustain topography for geological time, and is a natural outcome of the upwards advection which accompanies rifting.

An episode of active heating (for instance by shear) is attractive because it may explain the observation that bands develop from ridges (Prockter et al., 2002). Ridges at which shear-heating occurs will be warmer and thus weaker than the surrounding ice (Fig. 4a). If an extensional force is applied to an area containing such a ridge, the extension is likely to localize in the weakest area (see, e.g., Newman and White, 1999). Thus, the link between ridges and bands is easy to understand if ridges are sites of shear-heating. There is no need for shear-heating to be operating at the present day since, as described above, the heating-induced compositional buoyancy is permanent.

#### 4.2. Consequences of passive thermal support

As mentioned above, passive thermal support only works if the timescale over which rifting happens is short compared to the timescale of diffusive cooling, Eq. (5). The characteristic rifting timescale  $\tau_r \sim d/v$ , where  $v$  is the vertical advection velocity and  $d$  is a characteristic length scale. Together with Eq. (5), we obtain a Peclet-style relation:

$$v \gtrsim \kappa/d. \quad (8)$$

We will assume  $d$  is represented by the brittle-ductile transition depth, which is  $\approx 2$  km (Pappalardo et al., 1999; Nimmo and Gaidos, 2002). For  $\kappa = 10^{-6} \text{ m}^2 \text{ s}^{-1}$ ,  $v \gtrsim 10 \text{ mm yr}^{-1}$ . This velocity is comparable to that of slow-spreading ridges on Earth, and implies a band formation timescale of  $< 1$  Myr. As the bands examined here have been cross-cut by ridges or otherwise deformed (Prockter et al., 1999), these later deformational events must be even younger.

Another consequence of passive support is that younger bands would have higher topography than older bands. Thus, a correlation between band age and band topography would be strong evidence for a passive support mechanism. While stratigraphic analyses indicate that band-forming activity has waned with time (Prockter et al., 1999; Figueredo and Greeley, 2003), there is as yet no evidence of any trend in band topography with age.

#### 4.3. Elastic thickness estimates

The topography due to lateral density contrasts (irrespective of their origin) will be affected by the effective elastic thickness of the near-surface material. Figure 5 shows that elastic thicknesses in the range 0.1–1 km reproduce the observations reasonably well. Although these values are approximate, they broadly agree with some other  $T_e$  estimates (Tufts et al., 1997; Williams and Greeley, 1998; Billings and Kattenhorn, 2002), though they are smaller than other values (Figueredo et al., 2002; Nimmo et al., 2003). Since the  $T_e$  value recorded is the lowest since the load is emplaced, the  $T_e$  values derived here are probably representative of local conditions during band formation, and not necessarily those at the present day.

We also note that the existence of large values of near-surface porosity (Section 3.2.3) are likely to reduce the effective Young's modulus. Since flexural profiles directly constrain the rigidity, Eq. (3) shows that a reduction in Young's modulus  $E$  will result in an increase in the  $T_e$  value, and hence the ice shell thickness, obtained.

### 5. Summary and conclusions

We have investigated possible mechanisms for topographic support of pull-apart bands on Europa. Topographic support by shell thickness variations is not favored because of the rapidity with which lower crustal flow occurs (Section 3.1). The density contrasts required to produce the observed topography are  $\approx 5 \text{ kg m}^{-3}$  for a 20 km shell and  $\approx 50 \text{ kg m}^{-3}$  for a 2 km shell.

The bands may be higher because they are more heavily fractured than the surrounding areas. Such porosity could have been produced by extensional faulting or during the cyclic motion of the Tufts et al. (2000) model, and is the most likely mechanism for thin ( $\approx 2$  km) ice shells. For such shell thicknesses, surface porosity variations of order 20% are required; for a thicker ( $\approx 20$  km) shell, the variations need only be 5% or less. The presence of a high porosity, kilometers thick near-surface layer on Europa may have a significant impact on the depth to which future sounding radar systems can penetrate (Chyba et al., 1998; Eluszkiewicz, submitted).

Purely passive thermal support (a result of rifting) can only operate if all the bands are young,  $\lesssim 1$  Myr. This time is a small fraction of the nominal surface age of Europa, suggesting that this mechanism on its own is not likely. We think the most likely explanation for band topography is lateral variations of brine content; such variations would need to be prohibitively large ( $\approx 20\%$ ) in a 2 km thick ice shell, but need be only 2% (vertically averaged) in a 20 km thick shell. These variations may be caused by passive advection or shear-heating. If ridges are zones of shear-heating, they will be weaker than the surrounding areas and thus be natural sites for bands to initiate, as is observed.

## Acknowledgments

F.N. acknowledges the support of the Royal Society, R.P. that of NASA PGG grant NAG5-11616. We are grateful to Bill Moore for helpful discussions, and Patricio Figueredo and Kevin Williams for thorough reviews.

## Appendix A

We wish to consider lateral flow in an ice shell which is both non-Newtonian and has a temperature-dependent thermal conductivity. A very similar approach was adopted by Bird (1991), but he used a different temperature structure. The analysis here follows that of Nimmo and Stevenson (2001) and Nimmo (2003); further details may be obtained in the latter paper (hereafter N03).

The strain rate  $\dot{\epsilon}$  depends on the stress  $\tau_{xz}$  as follows:

$$\dot{\epsilon} = \frac{\partial v}{\partial z} = A |\tau_{xz}|^{n-1} \tau_{xz} e^{-Q/RT}, \quad (\text{A.1})$$

where  $v$  is horizontal velocity,  $A$ ,  $Q$ , and  $n$  are rheological parameters (Goldsby and Kohlstedt, 2001),  $R$  is the gas constant and  $T$  is absolute temperature.

Following the method of N03, the variation of viscosity  $\eta$  with depth may be linearized as follows:

$$\eta \approx \eta_b \exp(z/\delta), \quad (\text{A.2})$$

where

$$\delta = \frac{RT_b t_c}{Q \ln(T_b/T_s)}, \quad (\text{A.3})$$

$z$  is the height above the base of the shell,  $\eta_b$  is the viscosity at the base of the conducting shell,  $t_c$  is the conducting shell thickness,  $T_b$  is the temperature at the base of the layer and  $T_s$  is the surface temperature. The natural logarithm arises because the thermal conductivity of ice varies as  $1/T$  (Klinger, 1980).

For cases in which the ice shell is convecting, the bulk of the shell beneath a near-surface lid will be isoviscous and the effective channel thickness  $\delta$  will approach that of the shell thickness (e.g., McKinnon, 1999; Nimmo and Manga, 2002). Thus, the timescales derived below are likely to overestimate the timescales if convection is occurring. An additional complication in non-Newtonian cases is that the convective stresses may affect the viscosity of the material; this complication is not treated below.

Neglecting convection, horizontal flow in the lowermost part of the shell is driven by lateral pressure gradients. Assuming vertical flow is negligible, for an isostatically compensated case we have

$$\frac{\partial \tau_{xz}}{\partial z} = \frac{\partial P}{\partial x} = \Delta \rho g \frac{\partial t_c}{\partial x}, \quad (\text{A.4})$$

where  $P$  is pressure and  $\tau_{xz}$  is horizontal shear stress,  $t_c(x)$  is the shell thickness,  $g$  is gravity, and  $\Delta \rho$  is the density contrast between the shell and the underlying fluid.

Following Nimmo and Stevenson (2001), the variation of lateral flow velocity with depth is given by

$$v(z) = F \int_0^z |z' - \alpha|^{n-1} (z' - \alpha) e^{-z'/\delta} dz', \quad (\text{A.5})$$

where  $F = AE_b(\Delta \rho g \partial t_c / \partial x)^n$  and  $z$  is measured upwards from the base of the shell,  $E_b = \exp(-Q/RT_b)$ ,  $\alpha = (\tau_0 / \Delta \rho g) \partial t_c / \partial x$ , and  $\tau_0$  is the stress at the base of the shell. The constant  $\alpha$  is found from the requirement that  $v(\infty) = 0$  and gives the height at which the velocity is maximum.

We use continuity to obtain the rate of change of shell thickness, assuming that  $B$  and  $E_b$  do not vary with  $x$ :

$$\frac{dt_c}{dt} = -ABE_b \frac{d}{dx} \left| \Delta \rho g \frac{\partial t_c}{\partial x} \right|^{n-1} \Delta \rho g \frac{\partial t_c}{\partial x}, \quad (\text{A.6})$$

where

$$B = \int_0^\infty \int_0^z |z' - \alpha|^{n-1} (z' - \alpha) e^{-z'/\delta} dz' dz. \quad (\text{A.7})$$

For integer  $n$ , both  $\alpha$  and  $B$  may be derived in a relatively straightforward fashion from Eqs. (A.5) and (A.7) and the requirement that  $v(\infty) = 0$ . Obtaining  $\alpha$  requires the solution of an  $n$ th-order polynomial; solutions for even  $n$  are more complicated because of the  $||$ . Values of  $\alpha/\delta$  are 1.0, 1.3, 1.596 for  $n = 1, 2, 3$ , respectively (these values are the same as those given for  $k_1 b$  by Bird (1991)).

Although Eq. (A.6) is non-linear for  $n \neq 1$ , a reasonable approximation for the time constant of topographic decay  $\tau$  may be obtained by assuming that

$$\tau \approx \frac{-\Delta t_c}{\left. \frac{d\Delta t_c}{dt} \right|_{t=0}}, \quad (\text{A.8})$$

where  $\Delta t_c$  is the difference between the maximum and mean shell thickness.

For a sinusoidal variation in thickness of amplitude  $2\Delta t_c$  and wavelength  $\lambda$ , Eq. (A.6) gives

$$\frac{d\Delta t_c}{dt} = -\Delta t_c^n k^{n+1} n A B E_b (\Delta \rho g)^n, \quad (\text{A.9})$$

where  $k = 2\pi/\lambda$ . Using Eq. (A.8) and the result that  $B = \alpha^{n+1} \delta$  gives

$$\tau \approx (\Delta t_c^{n-1} k^{n+1} n A \alpha^{n+1} \delta E_b [\Delta \rho g]^n)^{-1}. \quad (\text{A.10})$$

For  $n = 1$  this expression reproduces the usual expression for the decay time of Newtonian fluids (e.g., N03). It also illustrates that, for non-Newtonian fluids, the decay time depends on the amplitude of the initial disturbance. For the same starting viscosity, a disturbance in a Newtonian fluid will decay faster than in a non-Newtonian one because in the latter the reduction in amplitude of the disturbance leads to an increase in effective viscosity.

We compared the results of Eq. (A.10) with those obtained by a numerical method (N03) for the initial topography to be reduced by a factor of  $\exp(1)$ . For  $n = 1$  the

timescales agreed; for  $1 < n < 3$  Eq. (A.10) underestimates the numerical timescale by a factor  $< 8$ , because of the non-linearity in (A.6).

## Appendix B

The rate of removal of porosity  $\phi$  due to viscous flow is given by Fowler (1985)

$$\frac{d\phi}{dt} = -\phi \frac{P}{\eta}, \quad (\text{B.1})$$

where  $P$  is the overburden pressure and  $\eta$  is the (Newtonian) viscosity of the medium. The porosity at any depth thus declines according to

$$\phi(z, t) = \phi_0(z) \exp(-t/\tau), \quad (\text{B.2})$$

where  $\phi_0(z)$  is the initial porosity structure and  $\tau$  is a time constant given by

$$\tau(z) = \frac{\eta(z)}{\rho g z}, \quad (\text{B.3})$$

where  $z$  is depth,  $\rho$  is density, and  $g$  is acceleration due to gravity. Assuming a Newtonian viscosity, we may write

$$\eta(z) = \eta_b \exp\left(\frac{Q}{R} \left[ \frac{1}{T(z)} - \frac{1}{T_b} \right]\right), \quad (\text{B.4})$$

where  $\eta_b$  and  $T_b$  are the viscosity and temperature at the base of the conductive part of the ice shell,  $Q$  is an activation energy, and  $R$  is the gas constant.

Assuming that the conductivity of ice varies as  $1/T$  (Klinger, 1980), the temperature profile within the conductive part of the ice shell is given by

$$T(z) = T_s \left( \frac{T_b}{T_s} \right)^{z/t_{\text{cond}}}, \quad (\text{B.5})$$

where  $t_{\text{cond}}$  is the thickness of the conductive part of the shell and  $T_s$  is the surface temperature.

Equations (B.2)–(B.5) may be used to obtain the vertical porosity profile (relative to its initial value) at any time, for a given ice rheology. A similar approach has been adopted by Eluszkiewicz (submitted), which gives broadly similar answers.

## References

Billings, S.E., Kattenhorn, S.A., 2002. Determination of ice crust thickness from flanking cracks along ridges on Europa. In: Proc. Lunar Planet. Sci. Conf. 33rd, p. 1813. Abstract.

Bird, P., 1991. Lateral extrusion of lower crust from under high topography in the isostatic limit. *J. Geophys. Res.* 96, 10275–10286.

Buck, L., Chyba, C.F., Goulet, M., Smith, A., Thomas, P., 2002. Persistence of thin ice regions in Europa's ice crust. *Geophys. Res. Lett.* 29, 2055.

Carlson, R.W., Johnson, R.E., Anderson, M.S., 1999. Sulfuric acid on Europa and the radiolytic sulfur cycle. *Science* 286, 97–99.

Chyba, C.F., Ostro, S.J., Edwards, B.C., 1998. Radar detectability of a subsurface ocean on Europa. *Icarus* 134, 292–302.

Eluszkiewicz, J. No prospect for detecting Europa's ocean by radar. *Icarus*. Submitted for publication.

Fanale, F.P., Li, Y.-H., De Carlo, E., Farley, C., Sharma, S.K., Horton, K., Granahan, J.C., 2001. An experimental investigation of Europa's "ocean" composition independent of Galileo orbital remote sensing. *J. Geophys. Res.* 106, 14595–14600.

Figueredo, P., Chuang, F.C., Rathbun, J., Kirk, R.L., Greeley, R., 2002. Geology and origin of Europa's "Mitten" feature (Murias Chaos). *J. Geophys. Res.* 107, 10.1029/2001JE001591.

Figueredo, P.H., Greeley, R., 2003. Resurfacing history of Europa from pole-to-pole geological mapping. *Icarus*. In press.

Fowler, A.C., 1985. A mathematical model of magma transport in the asthenosphere. *Geophys. Astrophys. Fluid Dynamics* 33, 63–96.

Gaidos, E.J., Nimmo, F., 2000. Tectonics and water on Europa. *Nature* 405, 637.

Geissler, P.E., et al., 1998. Evolution of lineaments on Europa: clues from Galileo multispectral imaging observations. *Icarus* 135, 107–126.

Giese, B., Oberst, J., Roatsch, T., Neukum, G., Head, J.W., Pappalardo, R.T., 1998. The local topography of Uruk Sulcus and Galileo Regio obtained from stereo images. *Icarus* 135, 303–316.

Goldsbey, D.L., Kohlstedt, D.L., 2001. Superplastic deformation of ice: experimental observations. *J. Geophys. Res.* 106, 11017–11030.

Greenberg, R., Geissler, P., Tufts, B.R., Hoppa, G.V., 2000. Habitability of Europa's crust: the role of tidal-tectonic processes. *J. Geophys. Res.* 105, 17551–17562.

Greenberg, R., Geissler, P., Hoppa, G., Tufts, B.R., 2002. Tidal-tectonic processes and their implications for the character of Europa's icy crust. *Rev. Geophys.* 40, 1–33.

Head, J.W., Pappalardo, R.T., Sullivan, R., 1999. Europa: morphological characteristics of ridges and triple bands from Galileo data (E4 and E6) and assessment of a linear diapirism model. *J. Geophys. Res.* 104, 24223–24236.

Hoppa, G.V., Tufts, B.R., Greenberg, R., Geissler, P.E., 1999. Formation of cycloidal features on Europa. *Science* 285, 1899–1902.

Kargel, J.S., Kaye, J.Z., Head, J.W., Marion, G.M., Sassen, R., Crowley, J.K., Ballesteros, O.P., Grant, S.A., Hogenboom, D.L., 2000. Europa's crust and ocean: origin, composition, and the prospects for life. *Icarus* 148, 226–265.

Kirk, R.L., Stevenson, D.J., 1987. Thermal evolution of a differentiated Ganymede and implications for surface features. *Icarus* 69, 91–134.

Kivelson, M.G., Khurana, K.K., Russel, C.T., Volwerk, M., Walker, R.J., Zimmer, C., 2000. Galileo magnetometer measurements: a stronger case for a subsurface ocean at Europa. *Science* 289, 1340–1342.

Klinger, J., 1980. Influence of a phase transition of ice on the heat and mass balance of comets. *Science* 209, 271–272.

Kossacki, K.J., Leliwa-Kopystynski, J., 1993. Medium-sized icy satellites—thermal and structural evolution during accretion. *Planet. Space Sci.* 41, 729–741.

Lucchitta, B.K., Soderblom, L.A., 1982. Geology of Europa. In: Morrison, D. (Ed.), *Satellites of Jupiter*. Univ. of Arizona Press, Tucson, pp. 521–555.

McCord, T.B., Hansen, G.B., Matson, D.L., Johnson, T.V., Crowley, J.K., Fanale, F.P., Carlson, R.W., Smythe, W.D., Martin, P.D., Hibbits, C.A., Granahan, J.C., Ocampo, A., 1999. Hydrated salt minerals on Europa's surface from the Galileo Near-Infrared Mapping Spectrometer (NIMS) investigation. *J. Geophys. Res.* 104, 11827–11851.

McKinnon, W.B., 1999. Convective instability in Europa's floating ice shell. *Geophys. Res. Lett.* 26, 951–954.

Moore, W.B., 2001. Coupling tidal dissipation and convection. *Bull. Am. Astron. Assoc.* 33, 1106.

Newman, R., White, N., 1999. The dynamics of extensional sedimentary basins: constraints from subsidence inversion. *Philos. Trans. R. Soc. London Ser. A* 357, 805–830.

Nimmo, F., 2003. Non-Newtonian topographic relaxation on Europa. *Icarus*. Submitted for publication.

Nimmo, F., Stevenson, D., 2001. Estimates of martian crustal thickness from viscous relaxation of topography. *J. Geophys. Res.* 106, 5085–5098.

- Nimmo, F., Manga, M., 2002. Causes, characteristics and consequences of convective diapirism on Europa. *Geophys. Res. Lett.* 29 (23), 2109.
- Nimmo, F., Giese, B., Pappalardo, R.T., 2003. Estimates of Europa's ice shell thickness from elastically-supported topography. *Geophys. Res. Lett.* 30 (5), 1233.
- Nimmo, F., Gaidos, E.J., 2002. Thermal consequences of strike-slip motion on Europa. *J. Geophys. Res.* 107 (E11), 5021.
- O'Brien, D.P., Geissler, P., Greenberg, R., 2002. A melt-through model for chaos formation on Europa. *Icarus* 156, 152–161.
- Ojakangas, G.W., Stevenson, D.J., 1989. Thermal state of an ice shell on Europa. *Icarus* 81, 220–241.
- Pappalardo, R.T., Head, J.W., Greeley, R., Sullivan, R.J., Pilcher, C., Schubert, G., Moore, W.B., Carr, M.H., Moore, J.M., Belton, M.J.S., Goldsby, D.L., 1998. Geological evidence for solid-state convection in Europa's ice shell. *Nature* 391, 365–368.
- Pappalardo, R.T., et al., 1999. Does Europa have a subsurface ocean? Evaluation of the geological evidence. *J. Geophys. Res.* 104, 24015–24055.
- Patterson, G.W., Head, J.W., 2003. Crustal spreading on Europa: inferring tectonic history from triple junction analysis. In: *Proc. Lunar Planet. Sci. Conf.* 34th, p. 1262. Abstract.
- Pierazzo, E., Chyba, C., 2002. Cometary delivery of biogenic elements to Europa. *Icarus* 157, 120–127.
- Prockter, L.M., Antman, A.M., Pappalardo, R.T., Head, J.W., Collins, G.C., 1999. Europa: stratigraphy and geological history of the anti-jovian region from Galileo E14 solid-state imaging data. *J. Geophys. Res.* 104 (E7), 16531–16540.
- Prockter, L.M., Head, J.W., Pappalardo, R.T., Sullivan, R.J., Clifton, A.E., Giese, B., Wagner, R., Neukum, G., 2002. Morphology of European bands at high resolution: a mid-ocean ridge-type rift mechanism. *J. Geophys. Res.* 107 (E5), 5028.
- Ross, M.N., Schubert, G., 1987. Tidal heating in an internal ocean model of Europa. *Nature* 325, 133–134.
- Sarid, A.R., Greenberg, R., Hoppa, G.V., Hurford, T.A., Tufts, B.R., Geissler, P., 2002. Polar wander and surface convergence of Europa's ice shell: evidence from a survey of strike-slip displacement. *Icarus* 158, 24–41.
- Schenk, P.M., 2002. Thickness constraints on the icy shells of the Galilean satellites from a comparison of crater shapes. *Nature* 417, 419–421.
- Schenk, P.M., McKinnon, W.B., 1989. Fault offsets and lateral crustal movement on Europa—evidence for a mobile ice shell. *Icarus* 79, 75–100.
- Schenk, P.M., McKinnon, W.B., 2001. Topographic variability on Europa from Galileo stereo images. In: *Proc. Lunar Planet. Sci. Conf.* 32nd, p. 2078. Abstract.
- Schulson, E.M., 2002. On the origin of a wedge crack within the icy crust of Europa. *J. Geophys. Res.* 107, 5107.
- Sotin, C., Head, J.W., Tobie, G., 2002. Europa: tidal heating of upwelling thermal plumes and the origin of lenticulae and chaos melting. *Geophys. Res. Lett.* 29, 1233.
- Stevenson, D.J., 2000. Limits on the variation of thickness of Europa's ice shell. In: *Proc. Lunar Planet. Sci. Conf.* 31st, p. 1506. Abstract.
- Sullivan, R., Greeley, R., Homan, K., Klemaszewski, J., Belton, M.J.S., Carr, M.H., Chapman, C.R., Tufts, R., Head, J.W., Pappalardo, R., Moore, J., Thomas, P., 1998. Episodic plate separation and fracture infill on the surface of Europa. *Nature* 391, 371–373.
- Tufts, R., Greenberg, R., Geissler, P., Hoppa, G., Pappalardo, R., Sullivan, R., 1997. Crustal displacement features on Europa. *Geol. Soc. Am. Abs. Prog.* 29, A-312.
- Tufts, B.R., Greenberg, R., Hoppa, G., Geissler, P., 2000. Lithospheric dilation on Europa. *Icarus* 146, 75–97.
- Turcotte, D.L., Schubert, G., 1982. *Geodynamics*. Wiley, New York.
- Turtle, E.P., Ivanov, B.A., 2002. Numerical simulations of impact crater excavation and collapse on Europa: implications for ice thickness. In: *Proc. Lunar Planet. Sci. Conf.* 33rd, p. 1431. Abstract.
- White, N., Bellingham, P., 2002. A two-dimensional inverse model for extensional sedimentary basins. 1. Theory. *J. Geophys. Res.* 107, 2259.
- Williams, K.K., Greeley, R., 1998. Estimates of ice thickness in the Conamara Chaos region of Europa. *Geophys. Res. Lett.* 25, 4273–4276.
- Wood, R., Barton, P.J., 1983. Crustal thinning and subsidence in the North Sea. *Nature* 302, 134–136.
- Zahnle, K., Schenk, P.M., Levison, H.F., Dones, L., 2003. Cratering rates in the outer Solar System. *Icarus* 163, 263–289.
- Zolotov, M.Y., Shock, E.L., 2001. Composition and stability of salts on the surface of Europa and their oceanic origin. *J. Geophys. Res.* 106, 32815–32827.